







Parametric instability in coupled nonlinear microcavitiesN. Carlon Zambon ¹, S. R. K. Rodriguez ^{1,2}, A. Lemaître ¹, A. Harouri,¹ L. Le Gratiet,¹
I. Sagnes,¹ P. St-Jean,¹ S. Ravets ¹, A. Amo ³ and J. Bloch ¹¹*Université Paris-Saclay, Centre National de la Recherche Scientifique,
Centre de Nanosciences et de Nanotechnologies, 91120 Palaiseau, France*²*Center for Nanophotonics, AMOLF, Science Park 104, 1098 XG Amsterdam, The Netherlands*³*Université de Lille, Centre National de la Recherche Scientifique, UMR 8523,
Physique des Lasers Atomes et Molécules, F-59000 Lille, France*

(Received 25 October 2019; revised 26 February 2020; accepted 13 July 2020; published 21 August 2020)

We report the observation of a parametric instability in the out-of-equilibrium steady state of two coupled Kerr microresonators coherently driven by a laser. Using a resonant excitation, we drive the system into an unstable regime, where we observe the appearance of intense and well-resolved sideband modes in the emission spectrum. This feature is a characteristic signature of self-sustained oscillations of the intracavity field. We comprehensively model our findings using semiclassical Langevin equations for the cavity field dynamics combined with a linear stability analysis. The inherent scalability of our semiconductor platform, enriched with a strong Kerr nonlinearity, is promising for the realization of integrated optical parametric oscillator networks.

DOI: [10.1103/PhysRevA.102.023526](https://doi.org/10.1103/PhysRevA.102.023526)**I. INTRODUCTION**

Nonlinear photonic systems, being inherently lossy, have been proposed as a natural playground for the exploration of out-of-equilibrium lattice models [1–4]. One example is the driven dissipative Bose-Hubbard (DDBH) model, describing interacting bosons hopping on a lattice in presence of pump and loss, where the emergent physics of dissipative phase transitions was recently investigated [5–11]. A minimal realization of this model is represented by two coupled nonlinear Kerr-type resonators. Despite its apparent simplicity, this paradigmatic system presents a rich phenomenology including spontaneous symmetry breaking [12], self-trapping and Josephson oscillations [13,14], periodic squeezing [15], and a nonlinear hopping phase [16]. Moreover, the interplay of fluctuations with nonlinearities is known to seed self-pulsing instabilities [17–20], which can be exploited to realize efficient integrated optical parametric oscillators [21–26].

Interestingly, the presence of such parametric instabilities was theoretically predicted for a DDBH dimer [27], finding a possible implementation in coupled microcavities hosting polariton excitations [28]. The mechanism responsible for the instability relates to the opening of a resonant scattering channel from the pump toward two modes, namely, the bonding and antibonding modes of the dimer, as their energy gets renormalized by the nonlinearity. Unlike previously demonstrated triply resonant schemes involving microcavity polaritons [29–33], in this paper the parametric instability involves just two polariton modes, the pump at threshold not being in resonance with any of them. This configuration not only prevents dephasing of the pump mode in the cavity via parametric luminescence [34], but also ensures excellent spatial overlap of the modes participating in the process. A

large parametric conversion efficiency is thus expected. In coupled microcavities, such instability has not been observed yet and when generalized to a lattice is expected to originate peculiar steady-state correlation properties [35].

Here we report the observation of a multimode parametric instability occurring within a hysteresis cycle of the population of two nonlinear coupled microresonators. This instability feeds sustained parametric oscillations, which we detect in energy-resolved measurements. Imaging the emission pattern of signal and idler modes in the instability regime, we evidence their opposite spatial symmetry. This feature is reminiscent of the bonding and antibonding linear modes from which they originate, supporting the description of the instability mechanism proposed in Ref. [27]. Our findings are supported by calculations based on a semiclassical coupled-mode description of the intracavity fields including vacuum fluctuations. As expected, the energy transfer from the pump to the parametrically excited modes is very efficient, with a sideband to pump intensity ratio as large as 0.38 for a submilliwatt threshold power. These figures of merit, combined with the scalability of a semiconductor platform, set a favorable ground for the exploration of few-photon chaotic instabilities [36,37] and dissipative time crystals [38–40] in lattices of microresonators and their relation with ergodicity in open systems [41].

II. LINEAR SPECTROSCOPY AND THE COUPLED-MODE MODEL

The coupled microcavities are fabricated starting from a planar semiconductor heterostructure grown by molecular-beam epitaxy. Two $\text{Al}_{0.10}\text{Ga}_{0.90}\text{As}/\text{Al}_{0.95}\text{Ga}_{0.05}\text{As}$ distributed Bragg reflectors separated by a GaAs λ spacer and embedding

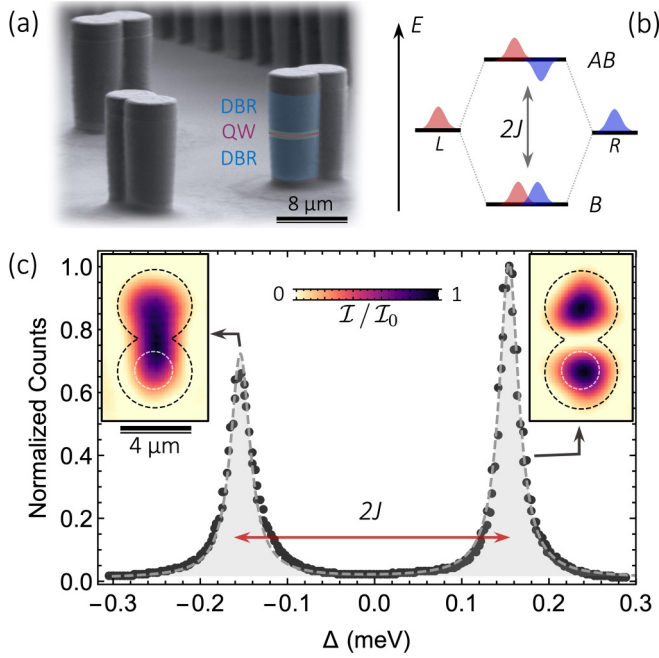


FIG. 1. (a) Scanning electron microscope image of the coupled micropillar cavities composed by two distributed Bragg reflectors (DBR), a λ spacer, and a quantum well (QW), shaded in blue, green, and purple, respectively. (b) Schematic representation of the hybridization of the two bare pillar modes into molecular bonding (B) and antibonding (AB) photonic modes. (c) Measured transmission as a function of the laser detuning relative to the uncoupled cavity resonance Δ . The dashed line is a fit with the Eq. (1) steady-state expectation value. The left and right insets show the transmission pattern measured at each resonance. The dashed lines indicate the edge of the microstructure and the half-maximum contour of the incident laser spot.

a single 15-nm $\text{In}_{0.05}\text{Ga}_{0.95}\text{As}$ quantum well form a Fabry-Pérot cavity operating in the strong light-matter coupling regime [28]. In order to avoid spurious Fabry-Pérot effects in the double polished substrate wafer, a silicon-oxynitride quarter-wave antireflective coating is deposited on its back face. At 4 K, the measured cavity finesse is $\mathcal{F} \approx 7 \times 10^4$, limited by residual absorption. The polariton dispersions in the as-grown sample are measured via energy and angle-resolved photoluminescence [42]. A coupled-mode model fit to the dispersion allows us to extract the Rabi splitting $\hbar\Omega_R = 3.39(4)$ meV and the bare exciton energy $E_x = 1454.78(3)$ meV. The wafer is finally processed with electron-beam lithography and inductively coupled plasma etching to fabricate microstructures consisting of two overlapping cylindrical resonators [see Fig. 1(a)]. In this paper the two resonators have a radius of $2.0 \mu\text{m}$ and a center-to-center distance of $3.6 \mu\text{m}$. When two micropillars overlap, their discrete eigenmodes hybridize, forming photonic molecular modes [43], as illustrated in Fig. 1(b). The energy separation between the two lowest eigenmodes (often called bonding and antibonding) is directly related to the spatial overlap between the pillars and can thus be adjusted by tuning their relative distance [44].

In transmission spectroscopy experiments, the sample is held at 4 K in a cryostat and probed using a single-mode tunable Ti:sapphire laser stabilized in power and frequency. The linear polarization of the excitation beam is aligned parallel to the long symmetry axis of the photonic molecule. A 0.55 NA microscope objective focuses the laser ($\approx 2 \mu\text{m}$ full width at half maximum) on one of the two micropillars. The transmitted intensity is collected with a second microscope objective and imaged on the entrance slit of a monochromator coupled to a CCD camera. The spectral resolution of the system is $\approx 40 \mu\text{eV}$.

The linear response of the coupled microcavities is first characterized by shining a weak pump laser and recording the transmitted intensity as a function of the laser detuning $\Delta = \hbar\omega_p - \hbar\omega_0$, where ω_p indicates the laser frequency and ω_0 the frequency of the fundamental mode of each (identical) pillar. The result is shown in Fig. 1(c). We observe two sharp resonances corresponding to the bonding and antibonding modes of the structure. The insets show an image of the transmission measured at each of the two resonances. The even (odd) spatial symmetry of these patterns indicates the bonding (antibonding) character of the modes.

In order to fit these results and extract the relevant parameters of the system within a coupled-mode description, we introduce a set of two Langevin equations for the complex amplitudes $\alpha_{1,2}$ of the polariton fields in each micropillar [45–47]. In the frame rotating at the pump frequency and setting $\hbar = 1$, the equations read

$$i d\alpha_{1,2} = (\mathcal{K}_{1,2} - J\alpha_{2,1})dt + d\chi_{1,2}(t),$$

$$\mathcal{K}_j = [-\Delta + U(|\alpha_j|^2 - 1) - i\gamma_j/2]\alpha_j + i\sqrt{\gamma/2}F_j. \quad (1)$$

Δ is the laser detuning relative to the bare cavity resonance, F_j is the on-site laser amplitude, γ is the polariton linewidth, U is the Kerr nonlinearity, J is the intercavity coupling constant, and $\chi_j(t)$ is a complex-valued Gaussian noise of variance $\langle \chi_j^*(t)\chi_j(t') \rangle = \delta_{j,j'}\delta(t-t')\gamma/2$. Only one cavity is driven in all the experiments: in this way, the excitation couples both to the linear B and AB modes of the coupled resonators. However, to model a slightly different coupling of the excitation spot with the dimer modes, we set $F_2 = \eta F_1$, where $\eta = -0.08$ and F_1 can be chosen real, without loss of generality. The dashed line in Fig. 1(c) is a fit of the stationary expectation value of Eq. (1) in the case of a weak drive (where the nonlinear terms are neglected). From the fit we obtain the polariton linewidth $\gamma = 27.4(8) \mu\text{eV}$, the coupling strength $J = 154.1(6) \mu\text{eV}$, and the fundamental mode energy $\hbar\omega_0 = 1450.64(1) \text{meV}$.

III. NONLINEAR RESPONSE

To probe the nonlinear response of the coupled microcavities, we tune the frequency of the laser at the antibonding resonance ($\Delta = J$). In Figs. 2(a) and 2(b) we show the measured polariton number $n_i = |\alpha_i|^2$ in each microcavity as a function of pump power. Hereafter subscript 1 (2) refers to the driven (undriven) cavity. Each data point has been extracted by imaging the transmitted intensity and integrating the counts over a region of interest corresponding to each of the micropillars [see the inset of Fig. 2(a)]. The count rates ($\phi_{1,2}$) are corrected

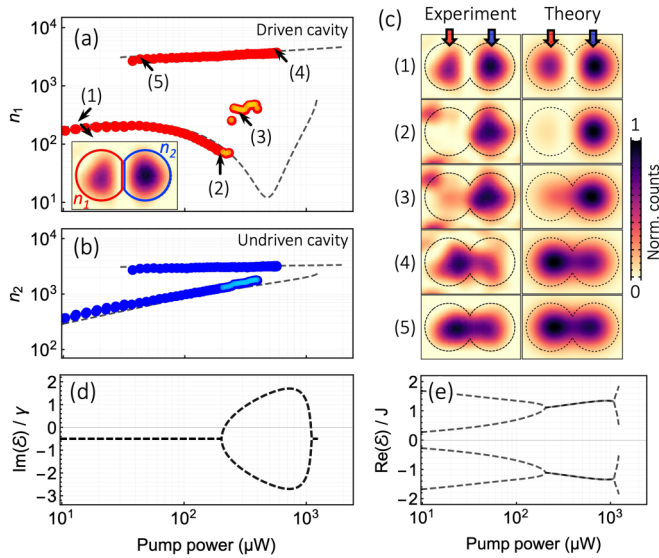


FIG. 2. (a, b) Symbols, measured polariton occupation number of the (a) driven and (b) undriven cavity, as a function of pump power; dashed line, steady-state prediction deduced from Eq. (1) with U being the only adjustable parameter. (c) Left panels: Intensity patterns measured at the five different pump powers indicated in panel (a). Right panels: Calculated intensity patterns obtained as time-averaged solutions of Eq. (1), multiplied with a Gaussian spatial profile. The spatial patterns in panels (c1) and (c5) correspond to near-resonant driving conditions of the linear antibonding and nonlinear bonding modes. (d, e) Imaginary and real parts of the stability matrix eigenvalues as a function of pump power, along the lower branch of the hysteresis cycle.

for detection efficiency and converted to a population using the relation $n_i = 2\tau\Phi_i|c_p|^{-2}$ where $\tau \approx 24$ ps is the polariton lifetime and $|c_p|^2 = 0.86(1)$ is the polariton photonic fraction at the frequency ω_0 . We observe [Figs. 2(a) and 2(b)] that the coupled cavity population exhibits a hysteretic behavior as the pump power is cycled between 40 and 400 μ W. Dashed lines correspond to the steady-state mean-field predictions (i.e., neglecting noise terms and setting $\dot{\alpha}_i = 0$) derived from Eq. (1) with U being the only adjustable parameter. We find the best agreement between experiments and theory for $U \approx 0.1$ μ eV, corresponding to an exciton-exciton interaction constant $g_{xx} \sim 30$ μ eV μ m², a result consistent with recent weak polariton blockade experiments [48,49]. Importantly, for $P > 200$ μ W along the lower branch of the hysteresis, the predictions of a steady-state model are inaccurate: this signals the onset of a dynamical feature investigated in detail in what follows.

The left column of Fig. 2(c) shows measured transmission patterns for five representative values of the pump power across the hysteresis cycle. At low power (1), since $\Delta = J$, the emission closely resembles the linear AB mode. Darkening of the driven cavity is observed in (2), due to an interference effect between the driving field and intracavity field of the coupled cavity. The phase of the undriven cavity depends on the pump power because of the coherent coupling (J) and the Kerr nonlinearity [16]. A small power increase (above $P_{\text{thr}} \approx 240$ μ W) produces an abrupt jump in the driven cavity population, as shown in (3). By further increasing the pump

power, we observe in (4) another jump in the transmitted intensity and a change to a bonding-type spatial profile, that persists throughout the upper branch of the bistability (5). The right column of Fig. 2(c), presents the corresponding theoretical predictions obtained by time averaging the long term dynamics of Eq. (1) after having adiabatically ramped the power to a specified value. Notice that in this simulation the effect of fluctuations of the intracavity field is included. The amplitudes $\langle \alpha_i \rangle_t$ are multiplied by a Gaussian spatial profile approximating the uncoupled pillar modes. The resulting intensity maps are in excellent agreement with the experimental observations, showing that, when including fluctuations, we can fully reproduce the data in Fig. 2(a).

To further understand the behavior of the system along the lower bistability branch, we address the linear stability of the stationary solutions [27]. The imaginary and real parts of the eigenvalues of the stability matrix corresponding to the lower branch of the bistability are plotted in Figs. 2(d) and 2(e), respectively. The imaginary part indicates whether small perturbations around the stationary solutions are damped [$\text{Im}(\mathcal{E}) < 0$] or amplified [$\text{Im}(\mathcal{E}) > 0$]. When the pump power reaches ≈ 200 μ W, the imaginary part of the eigenvalues bifurcates with two of them becoming positive for $P > P_{\text{thr}}$, signaling the onset of an instability. Correspondingly, their real part collapses around $\pm J$ indicating an oscillating behavior of the perturbations. These are both characteristic features of a parametric instability [20]. Points fulfilling this condition in Figs. 2(a) and 2(b) are marked with a lighter dot.

To clarify the mechanism underlying this parametric instability, we present in Fig. 3(a) the total interaction energy $U(n_1 + n_2)$ as a function of pump power, deduced from the measured polariton occupation along the lower branch of the bistability. This quantity represents the energy shift of the eigenmode energies induced by interactions. Interestingly, when approaching the instability region starting around P_{thr} this energy shift becomes close to J . A resonant two-polariton scattering channel thus opens from the pump into the nonlinear bonding and antibonding modes, now symmetrically spaced in energy with respect to the pump.

IV. PARAMETRIC INSTABILITY: SPECTRAL SIGNATURES

The spectrally resolved transmission of the coupled microcavities while scanning forward and backward the input power across the bistability is shown in Figs. 3(b) and 3(c), respectively. In these measurements, the imaging system has been coupled to the entrance slit of a monochromator spatially aligned with the dimer axis [see inset in Fig. 3(b)]. For three power values, we display in Figs. 3(d)–3(f) the spatially and spectrally resolved measured patterns. For a pump power below the instability region $P < P_{\text{thr}}$, the spectrum in Fig. 3(b) is single toned. Since the pump is closer in energy to the antibonding resonance, it couples preferentially to this mode through its finite linewidth. Therefore, the corresponding spatial profile has an antibonding symmetry, clearly indicated by the intensity node at the center [see Fig. 3(d)]. As the pump power reaches P_{thr} , two well-resolved sidebands displaced by $\delta E = \pm 0.14(1)$ meV about the pump energy (E_p) appear. This is a clear signature of the sustained parametric

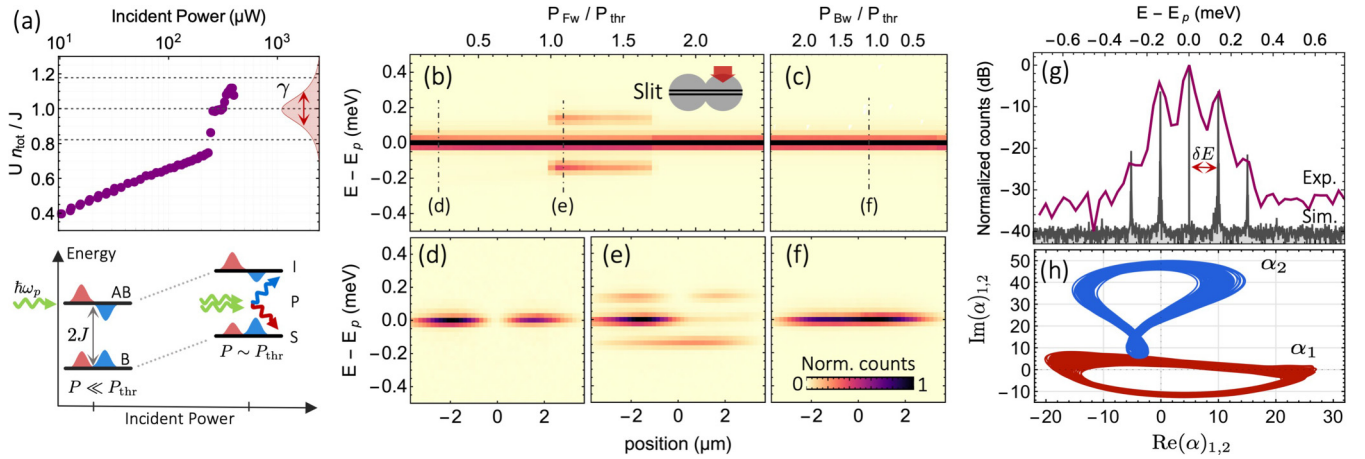


FIG. 3. (a) Total interaction energy $U n_{\text{tot}}$ deduced from the experiment as a function of the incident pump power along the lower bistability branch. Horizontal dashed lines correspond to $U n_{\text{tot}} = (J - \gamma, J, J + \gamma)$. Inset: Schematics of the parametric instability mechanism occurring as the bonding (B) and antibonding (AB) modes are blueshifted by interactions. (b, c) Integrated spectrally resolved emission of the microstructure measured while (b) increasing or (c) decreasing the pump power P_{Fw} (P_{Bw}), expressed in units of P_{thr} . (d-f) Position and energy resolved emission patterns (d) below, (e) within, and (f) well above the instability region. As schematized in panel (b), the spatial profile corresponds to a cut through the long symmetry axis of the structure, while the laser drives the right microcavity. (g) Measured (purple) and simulated (gray) emission spectrum of the coupled cavities at $1.1 P_{\text{thr}}$. (h) Calculated trajectories of the cavity field amplitudes $\alpha_{1,2}$ showing a limit cycle behavior in the instability region (2.5-ns evolution).

oscillations triggered by the instability, with the pump coherently exciting signal and idler fields. The corresponding spatially resolved pattern in Fig. 3(e) demonstrates that the lower (higher) energy sideband has a bonding (antibonding) symmetry, thus supporting the intuitive picture presented in Fig. 3(a). When the input power exceeds $1.7 P_{\text{thr}}$, the microcavity mode switches to the upper branch of the bistability. Along this branch the emission is monochromatic, as evidenced by the measured spectra in the backward power scan [Fig. 3(c)] and confirmed by a stability analysis of the upper branch solutions. The emission pattern is characterized by a bonding-type symmetry [see Fig. 3(f)]. Notice that a parametric instability was also theoretically predicted in Ref. [16]. However, in this experiment, the branches of the multistability could be continuously and reversibly explored, a behavior which is only possible if parametric processes are strongly suppressed. In this sense, we suspect that dephasing induced by slight heating of the sample played a key role.

Figure 3(g) presents in log scale the spatially integrated spectrum measured at $1.1 P_{\text{thr}}$. In addition to the bright signal and idler peaks, additional sidebands arising from higher-order scattering processes are clearly resolved; the width of all sideband peaks is resolution limited. The simulated spectrum (gray line), faithfully reproducing the sideband magnitudes, is the power spectral density of the cavity field dynamics computed via Eq. (1). Note that in order to match the spectral position of the peaks we have to rescale the energy axis of the simulation by a factor 0.86. This discrepancy can be ascribed to the fact that the coupling strength J , proportional to the overlap of the bare pillar eigenmodes, is slightly reduced when increasing the pump power, as interactions can modify their spatial profiles [27]. The presence of sidebands implies that the cavity fields ($\alpha_{1,2}$) display limit cycle dynamics in phase space, as shown by simulations in Fig. 3(h), with period

$\hbar/\delta E = 29(3)$ ps. Importantly, the energy fraction stored in the main sidebands is found to be as large as $I_{\text{sb}}/I_{\text{tot}} = 0.38$. Such an efficient parametric process is possible despite the absence of a triply resonant condition in our experimental scheme, because the parametric gain ($\approx U n_{\text{tot}}$) at threshold, i.e., when $U n_{\text{tot}} \approx \Delta \approx 5.5\gamma$ [see Fig. 3(a)], is more than five times larger than the losses. The combination of a moderate oscillation threshold ($P_{\text{thr}} \approx 240 \mu\text{W}$, or $n_{\text{thr}} \approx 1.5 \times 10^3$ polaritons) with a large sideband intensity evidences the potential of a polariton-based platform for the implementation of integrated optical parametric oscillator networks.

V. CONCLUSION

We demonstrate a multimode parametric instability within the hysteresis cycle of two coupled microresonators operating in the exciton-photon strong-coupling regime. The mechanism at the heart of the instability, namely, the opening of a resonant scattering channel from the pump towards a bonding-like signal and antibonding-like idler modes, is experimentally confirmed by individually resolving their spatial profile. All the observations are comprehensively modeled using a coupled-mode description of the intracavity fields including vacuum fluctuations. Given the generality of the instability mechanism and profiting from the inherent scalability of a semiconductor platform, we envisage the observation of similar parametric instabilities in lattices of microcavities presenting modes with a macroscopic degeneracy [50], chiral circulation [51], or nontrivial topological features [52–55]. Moreover, thanks to the hybrid light-matter nature of polariton excitations the system is endowed with a strong Kerr nonlinearity allowing us to observe the instability at few hundred microwatt threshold powers. In this direction, recent works demonstrating an order-of-magnitude enhancement of

U [56–58] encourage the investigation of optical parametric oscillators operating in the few photon regime [59]. Interestingly, dynamical instabilities also develop when two or more polariton condensates present simultaneously coherent and dissipative coupling terms [60,61]. The recent demonstration of an optical control over the coupling amplitudes in condensate lattices [62] offers a complementary playground for the investigation of synchronization and pattern formation [63]. In this context, our results may provide a simple rule of thumb to predict the presence of instabilities based on the energetic landscape and coupling strengths in condensate networks. Finally, as GHz phonons are also confined in AlGaAs based micropillar structures [64,65], one could exploit these parametric processes to excite and probe acoustic modes in polariton microcavities.

ACKNOWLEDGMENTS

The authors acknowledge stimulating discussions with Iacopo Carusotto and Alejandro Fainstein. This work was supported by the French National Research Agency (ANR) project Quantum Fluids of Light (Grant No. ANR-16-CE30-0021), the H2020-FETFLAG project PhoQus (Grant No. 820392), the French RENATECH network, the QUANTERA project Interpol (Grant No. ANR-QUAN-0003-05), the CPER Photonics for Society P4S, and the Métropole Européenne de Lille via the project TFlight. S.R.K.R. acknowledges the Netherlands Organisation for Scientific Research (NWO), a Marie Curie individual fellowship, and a NWO Veni grant (Project No. 680-47-457).

APPENDIX: LIMIT CYCLE DYNAMICS AND THE INFLUENCE OF FLUCTUATIONS

Here we present the complementary time-domain evolution of the intracavity field within the parametric instability region and address the influence of intrinsic vacuum fluctuations on the parametric oscillations. The starting point is the coupled Langevin Eq. (1). Notice that in absence of the noise terms $\chi_j(t)$ these Langevin equations reduce to the driven-dissipative Gross-Pitaevskii equation (DDGPE) for two coupled polariton modes [47]. In the following we use Eq. (1) to calculate the temporal dynamics of the coupled microcavity system for a monochromatic driving at a detuning $\Delta = J$, i.e., at the linear antibonding resonance of the system. The system is always initialized in the vacuum state: a 1.5-ns adiabatic power ramp brings the system into the parametric instability region, stabilizing at $P = 1.1P_{\text{thr}}$ (P_{thr} is the instability threshold). In order to compare time and frequency domain results, we calculate the temporal dynamics of the site-resolved cavity population, the associated power spectral density and trace the dynamics of the complex amplitudes $\alpha_{1,2}(t)$ in phase space.

In Figs. 4(a)–4(c) we show the results corresponding to the DDGPE evolution, that is, neglecting the noise terms in Eq. (1). Figure 4(a) shows the dynamics of the driven (red lines, $n_1 = |\alpha_1|^2$) and undriven (blue lines, $n_2 = |\alpha_2|^2$) cavity population. Notice that in absence of noise we need to trigger the instability adding a weak perturbation to the adiabatic power ramp (gray line) in the form of a 2-ps pulse (see the

inset). After the arrival of the perturbation, n_1 and n_2 start to oscillate with growing amplitude: following a short transient the system reaches a self-pulsing dynamical steady state ($t > 2.5$ ns). In Fig. 4(a) we also present a 200-ps snapshot of the evolution of n_1 and n_2 , from which we infer the period of the oscillations $T \approx 24$ ps. When we calculate in Fig. 4(b) the normalized power spectral density associated to the $t > 2.5$ ns dynamics of $\alpha_{1,2}$, the oscillating behavior manifests in well-resolved contrasted sidebands separated by $\delta E = h/T \approx 0.17$ meV. Such oscillation frequency corresponds to the real part of the parametrically unstable eigenvalues of the linear stability matrix at $P = 1.1P_{\text{thr}}$ [see Fig. 2(e) in the main text] and is roughly equal to the intercavity coupling constant J . In Fig. 4(c) we plot the evolution of the complex field amplitudes $\alpha_{1,2}$ in the dynamical steady state ($t > 2.5$ ns). As expected, we observe that in the frame rotating at the pump frequency the coherent parametric oscillations are associated to a limit cycle dynamics of $\alpha_{1,2}$. As we deal with a large but finite number of excitations at the instability threshold $\langle n_{\text{tot}} \rangle = \langle n_1 + n_2 \rangle \approx 1.5 \times 10^3 \sim \Delta/U$, the role of fluctuations cannot in principle be neglected. Indeed, intrinsic fluctuations in the system not only seed the instability but might affect the coherent oscillating dynamics of the intracavity fields. In order to address this question, we repeat the simulations presented in Figs. 4(a)–4(c) using Eq. (1) (including noise terms). This corresponds to the calculation presented in Figs. 3(g) and 3(h) in the main text.

The results are presented in Figs. 4(d)–4(f). Panel (d) shows the dynamics of the driven (red lines) and undriven (blue lines) cavity population. Here, there is no need to add any perturbation to the power ramp, as intrinsic fluctuations trigger the instability. Once the dynamical steady state of the system has set in, we observe again an oscillating behavior of $n_{1,2}$. The period of the oscillation is the same as in panel (a), but now the amplitude randomly oscillates from cycle to cycle. Figure 4(e) shows the normalized power spectral density associated to the last 2.5 ns of the stochastic evolution (gray line). As a reference we overlay the corresponding spectrum (red line) obtained for the DDGPE in panel (b). We see that the position of the sidebands is the same, confirming that the oscillation period is preserved, but the sideband height is slightly reduced. This is because fluctuations induce random phase shifts from cycle to cycle, leading to a dephasing of the oscillations over time [40]. The dynamics of $\alpha_{1,2}$ obtained via Eq. (1) is sampled every ps and shown as a scatterplot (gray dots) in Fig. 4(f). For comparison, we trace the corresponding limit cycle dynamics obtained via the DDGPE with solid lines. We can see that the stochastic dynamics associated to Eq. (1) produces a wandering of the limit cycle dynamics about the DDGPE predictions.

Since the noise term in Eq. (1) has constant variance $\gamma/2$ we can expect that, for smaller expectation values $\langle \alpha_{1,2} \rangle$ in the dynamical steady state, the effect of fluctuations becomes relatively more important. As the parametric instability is triggered when $n_{\text{tot}} \sim \Delta/U$, we can verify this intuition by repeating the simulation presented in Figs. 4(d)–4(f) for a factor 10 larger value of $U' = 10U = 1 \mu\text{eV}$ and correspondingly rescaling the input power $P' = P/10$. The results of this analysis are shown in Figs. 4(g)–4(i). Overall, from Figs. 4(g)–4(i), we conclude that the self-pulsing behavior is preserved

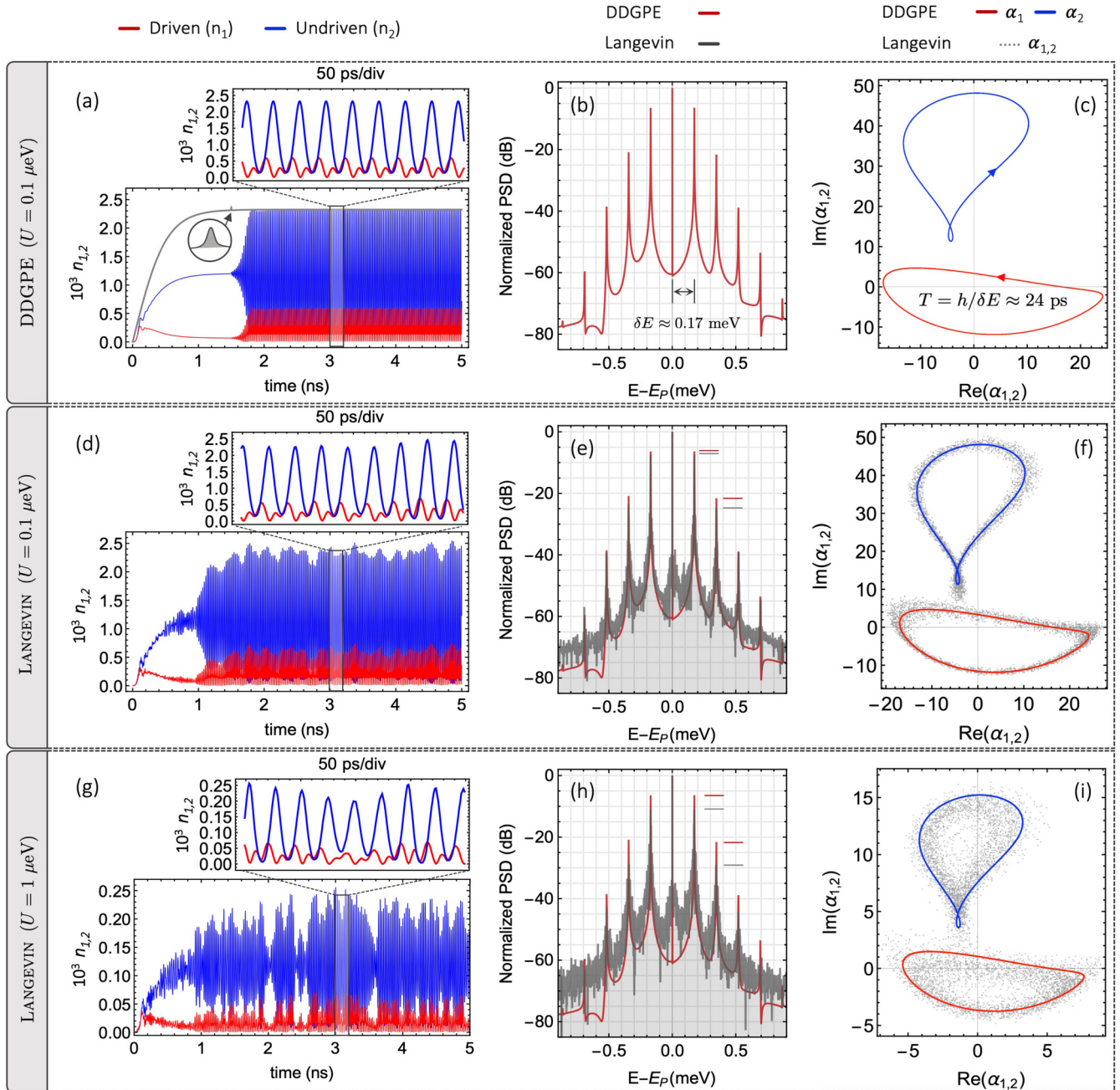


FIG. 4. Self-pulsing dynamics. (a–c) Simulations obtained using the generalized Gross-Pitaevskii equation for the coupled polariton modes, i.e., Eq. (1) in the absence of noise terms. (d–i) Simulations obtained via the coupled Langevin equations Eq. (1). (a, d, g) Dynamics of the driven (red line) and undriven (blue) cavity populations obtained with (a) the DDGPE for $U = 0.1 \mu\text{eV}$, (d) Eq. (1) for $U = 0.1 \mu\text{eV}$, and (g) Eq. (1) for $U = 10U = 1 \mu\text{eV}$. The first 1.5 ns of the dynamics are used to adiabatically ramp the pump power to $1.1P_{\text{thr}}$, [see gray line in panel (a)]. In the insets of panels (a), (d), and (g), we show a 200-ps snapshot of the dynamics, showing a self-pulsing behavior with period $T \approx 24$ ps. (b, e, h) Normalized power spectral density associated to the last 2.5-ns evolution of the cavity field dynamics shown in panels (a), (d), and (g), respectively. In panels (e) and (h) we keep plotting the DDGPE results obtained in panel (b) for comparison (solid red line). We can observe that the energy spacing of the sidebands ($\delta E \approx 0.17$ meV) remains unaffected by fluctuations; however, the relative height of the peaks decreases for larger fluctuations of the intracavity field (i.e., increasing U). (c, f, i) Phase-space limit cycle dynamics of the intracavity fields associated to the last 2.5-ns evolution shown in panels (a), (d), and (g), respectively. In panels (c), (f), and (i) the red and blue lines correspond to the driven and undriven cavity field dynamics computed via the DDGPE. Gray dots in panels (f) and (i) correspond to the stochastic dynamics obtained via Eq. (1) sampled every ps for $U = 0.1$ and $1 \mu\text{eV}$, respectively. As U increases the number of excitations in the cavity at the threshold decreases; thus the relative amplitude of the fluctuation increases, as shown by the scatterplot of the dynamics. The random phase shifts induced by fluctuations tend to dephase the parametric oscillations, thus reducing the temporal coherence of the process as the reduced sideband contrast in panels (e) and (h) indicates.

when decreasing the number of excitations at threshold and that the period of the oscillations remains constant. However, random phase shifts between the oscillation cycles become

more important; as a result the sideband contrast in the normalized power spectral density is progressively reduced [see Fig. 4(h)].

-
- [1] A. D. Greentree, C. Tahan, J. H. Cole, and L. C. L. Hollenberg, *Nat. Phys.* **2**, 856 (2006).
- [2] M. J. Hartmann, F. G. S. L. Brandão, and M. B. Plenio, *Nat. Phys.* **2**, 849 (2006).
- [3] D. G. Angelakis, M. F. Santos, and S. Bose, *Phys. Rev. A* **76**, 031805(R) (2007).
- [4] D. Gerace, H. E. Türeci, A. Imamoglu, V. Giovannetti, and R. Fazio, *Nat. Phys.* **5**, 281 (2009).
- [5] H. J. Carmichael, *Phys. Rev. X* **5**, 031028 (2015).
- [6] M. Foss-Feig, P. Niroula, J. T. Young, M. Hafezi, A. V. Gorshkov, R. M. Wilson, and M. F. Maghrebi, *Phys. Rev. A* **95**, 043826 (2017).
- [7] M. Biondi, G. Blatter, H. E. Türeci, and S. Schmidt, *Phys. Rev. A* **96**, 043809 (2017).
- [8] M. Fitzpatrick, N. M. Sundaresan, A. C. Li, J. Koch, and A. A. Houck, *Phys. Rev. X* **7**, 011016 (2017).
- [9] S. R. K. Rodriguez, W. Casteels, F. Storme, N. Carlon Zambon, I. Sagnes, L. Le Gratiet, E. Galopin, A. Lemaître, A. Amo, C. Ciuti, and J. Bloch, *Phys. Rev. Lett.* **118**, 247402 (2017).
- [10] T. Fink, A. Schade, S. Höfling, C. Schneider, and A. Imamoglu, *Nat. Phys.* **14**, 365 (2018).
- [11] F. Vicentini, F. Minganti, R. Rota, G. Orso, and C. Ciuti, *Phys. Rev. A* **97**, 013853 (2018).
- [12] P. Hamel, S. Haddadi, F. Raineri, P. Monnier, G. Beaudoin, I. Sagnes, A. Levenson, and A. M. Yacomotti, *Nat. Photonics* **9**, 311 (2015).
- [13] K. G. Lagoudakis, B. Pietka, M. Wouters, R. André, and B. Deveaud-Plédran, *Phys. Rev. Lett.* **105**, 120403 (2010).
- [14] M. Abbarchi, A. Amo, V. G. Sala, D. D. Solnyshkov, H. Flayac, L. Ferrier, I. Sagnes, E. Galopin, A. Lemaître, G. Malpuech, and J. Bloch, *Nat. Phys.* **9**, 275 (2013).
- [15] A. F. Adiyatullin, M. D. Anderson, H. Flayac, M. T. Portella-Oberli, F. Jabeen, C. Ouellet-Plamondon, G. C. Sallen, and B. Deveaud, *Nat. Commun.* **8**, 1329 (2017).
- [16] S. R. K. Rodriguez, A. Amo, I. Sagnes, L. Le Gratiet, E. Galopin, A. Lemaître, and J. Bloch, *Nat. Commun.* **7**, 11887 (2016).
- [17] L. A. Orozco, A. T. Rosenberger, and H. J. Kimble, *Phys. Rev. Lett.* **53**, 2547 (1984).
- [18] L. A. Lugiato, C. Oldano, C. Fabre, E. Giacobino, and R. J. Horowicz, *Il Nuovo Cimento D* **10**, 959 (1988).
- [19] M. Marconi, F. Raineri, A. Levenson, A. M. Yacomotti, J. Javaloyes, S. H. Pan, A. E. Amili, and Y. Fainman, *Phys. Rev. Lett.* **124**, 213602 (2020).
- [20] M. C. Cross and P. C. Hohenberg, *Rev. Mod. Phys.* **65**, 851 (1993).
- [21] T. J. Kippenberg, S. M. Spillane, and K. J. Vahala, *Phys. Rev. Lett.* **93**, 083904 (2004).
- [22] P. Del'Haye, A. Schliesser, O. Arcizet, T. Wilken, R. Holzwarth, and T. J. Kippenberg, *Nature (London)* **450**, 1214 (2007).
- [23] B. J. M. Hausmann, I. Bulu, V. Venkataraman, P. Deotare, and M. Lončar, *Nat. Photonics* **8**, 369 (2014).
- [24] A. Dutt, K. Luke, S. Manipatruni, A. L. Gaeta, P. Nussenzveig, and M. Lipson, *Phys. Rev. Appl.* **3**, 044005 (2015).
- [25] M. Pu, L. Ottaviano, E. Semenova, and K. Yvind, *Optica* **3**, 823 (2016).
- [26] X. Ji, F. A. S. Barbosa, S. P. Roberts, A. Dutt, J. Cardenas, Y. Okawachi, A. Bryant, A. L. Gaeta, and M. Lipson, *Optica* **4**, 619 (2017).
- [27] D. Sarchi, I. Carusotto, M. Wouters, and V. Savona, *Phys. Rev. B* **77**, 125324 (2008).
- [28] C. Weisbuch, M. Nishioka, A. Ishikawa, and Y. Arakawa, *Phys. Rev. Lett.* **69**, 3314 (1992).
- [29] R. M. Stevenson, V. N. Astratov, M. S. Skolnick, D. M. Whittaker, M. Emam-Ismael, A. I. Tartakovskii, P. G. Savvidis, J. J. Baumberg, and J. S. Roberts, *Phys. Rev. Lett.* **85**, 3680 (2000).
- [30] P. G. Savvidis, J. J. Baumberg, R. M. Stevenson, M. S. Skolnick, D. M. Whittaker, and J. S. Roberts, *Phys. Rev. Lett.* **84**, 1547 (2000).
- [31] C. Diederichs, J. Tignon, G. Dasbach, C. Ciuti, A. Lemaître, J. Bloch, P. Roussignol, and C. Delalande, *Nature (London)* **440**, 904 (2006).
- [32] M. Romanelli, C. Leyder, J. P. Karr, E. Giacobino, and A. Bramati, *Phys. Rev. Lett.* **98**, 106401 (2007).
- [33] L. Ferrier, S. Pigeon, E. Wertz, M. Bamba, P. Senellart, I. Sagnes, A. Lemaître, C. Ciuti, and J. Bloch, *Appl. Phys. Lett.* **97**, 031105 (2010).
- [34] C. Ciuti, P. Schwendimann, and A. Quattropani, *Phys. Rev. B* **63**, 041303(R) (2001).
- [35] A. Le Boité, G. Orso, and C. Ciuti, *Phys. Rev. Lett.* **110**, 233601 (2013).
- [36] K. Ikeda, *Opt. Commun.* **30**, 257 (1979).
- [37] D. D. Solnyshkov, R. Johne, I. A. Shelykh, and G. Malpuech, *Phys. Rev. B* **80**, 235303 (2009).
- [38] F. M. Gambetta, F. Carollo, M. Marcuzzi, J. P. Garrahan, and I. Lesanovsky, *Phys. Rev. Lett.* **122**, 015701 (2019).
- [39] C. Lledó, T. K. Mavrogordatos, and M. H. Szymańska, *Phys. Rev. B* **100**, 054303 (2019).
- [40] K. Seibold, R. Rota, and V. Savona, *Phys. Rev. A* **101**, 033839 (2020).
- [41] M. Žnidarič, T. Prosen, G. Benenti, G. Casati, and D. Rossini, *Phys. Rev. E* **81**, 051135 (2010).
- [42] R. Houdré, C. Weisbuch, R. P. Stanley, U. Oesterle, P. Pellandini, and M. Ilegems, *Phys. Rev. Lett.* **73**, 2043 (1994).
- [43] M. Galbiati, L. Ferrier, D. D. Solnyshkov, D. Tanese, E. Wertz, A. Amo, M. Abbarchi, P. Senellart, I. Sagnes, A. Lemaître, E. Galopin, G. Malpuech, and J. Bloch, *Phys. Rev. Lett.* **108**, 126403 (2012).
- [44] S. Michaelis de Vasconcellos, A. Calvar, A. Dousse, J. Suffczyński, N. Dupuis, A. Lemaître, I. Sagnes, J. Bloch, P. Voisin, and P. Senellart, *Appl. Phys. Lett.* **99**, 101103 (2011).
- [45] H. J. Carmichael, *Statistical Methods in Quantum Optics*, Theoretical and Mathematical Physics, Vol. 123, 1st ed. (Springer-Verlag, Berlin, 1999), Vol. 1.

- [46] I. Carusotto and C. Ciuti, *Phys. Rev. B* **72**, 125335 (2005).
- [47] I. Carusotto and C. Ciuti, *Rev. Mod. Phys.* **85**, 299 (2013).
- [48] A. Delteil, T. Fink, A. Schade, S. Höfling, C. Schneider, and A. İmamoğlu, *Nat. Materials* **18**, 219 (2019).
- [49] G. Muñoz-Matutano, A. Wood, M. Johnsson, X. Vidal, B. Q. Baragiola, A. Reinhard, A. Lemaître, J. Bloch, A. Amo, G. Nogues, B. Besga, M. Richard, and T. Volz, *Nat. Materials* **18**, 213 (2019).
- [50] C. E. Whittaker, E. Cancellieri, P. M. Walker, D. R. Gulevich, H. Schomerus, D. Vaitiekus, B. Royall, D. M. Whittaker, E. Clarke, I. V. Iorsh, I. A. Shelykh, M. S. Skolnick, and D. N. Krizhanovskii, *Phys. Rev. Lett.* **120**, 097401 (2018).
- [51] N. Carlon Zambon, P. St-Jean, M. Milićević, A. Lemaître, A. Harouri, L. Le Gratiet, O. Bleu, D. D. Solnyshkov, G. Malpuech, I. Sagnes, S. Ravets, A. Amo, and J. Bloch, *Nat. Photonics* **13**, 283 (2019).
- [52] T. Karzig, C.-E. Bardyn, N. H. Lindner, and G. Refael, *Phys. Rev. X* **5**, 031001 (2015).
- [53] A. V. Nalitov, D. D. Solnyshkov, and G. Malpuech, *Phys. Rev. Lett.* **114**, 116401 (2015).
- [54] S. Klembt, T. H. Harder, O. A. Egorov, K. Winkler, R. Ge, M. A. Bandres, M. Emmerling, L. Worschech, T. C. H. Liew, M. Segev, C. Schneider, and S. Höfling, *Nature (London)* **562**, 552 (2018).
- [55] S. Mittal, E. A. Goldschmidt, and M. Hafezi, *Nature (London)* **561**, 502 (2018).
- [56] E. Togan, H.-T. Lim, S. Faelt, W. Wegscheider, and A. Imamoglu, *Phys. Rev. Lett.* **121**, 227402 (2018).
- [57] I. Rosenberg, D. Liran, Y. Mazuz-Harpaz, K. West, L. Pfeiffer, and R. Rapaport, *Sci. Adv.* **4**, eaat8880 (2018).
- [58] P. Knüppel, S. Ravets, M. Kroner, S. Fält, W. Wegscheider, and A. Imamoglu, *Nature (London)* **572**, 91 (2019).
- [59] Z. Wang, M. Pechal, E. A. Wollack, P. Arrangoiz-Arriola, M. Gao, N. R. Lee, and A. H. Safavi-Naeini, *Phys. Rev. X* **9**, 021049 (2019).
- [60] K. Rayanov, B. L. Altshuler, Y. G. Rubo, and S. Flach, *Phys. Rev. Lett.* **114**, 193901 (2015).
- [61] S. Kim, Y. G. Rubo, T. C. H. Liew, S. Brodbeck, C. Schneider, S. Höfling, and H. Deng, *Phys. Rev. B* **101**, 085302 (2020).
- [62] S. Alyatkin, J. D. Töpfer, A. Askitopoulos, H. Sigurdsson, and P. G. Lagoudakis, *Phys. Rev. Lett.* **124**, 207402 (2020).
- [63] K. P. Kalinin and N. G. Berloff, *Phys. Rev. B* **100**, 245306 (2019).
- [64] A. Fainstein, N. D. Lanzillotti-Kimura, B. Jusserand, and B. Perrin, *Phys. Rev. Lett.* **110**, 037403 (2013).
- [65] J. Restrepo, C. Ciuti, and I. Favero, *Phys. Rev. Lett.* **112**, 013601 (2014).